ACS NANO

Cite This: ACS Nano 2018, 12, 8104–8114

www.acsnano.org

ARTICLE

Effective Neural Photostimulation Using Indium-Based Type-II Quantum Dots

Houman Bahmani Jalali,[†] Mohammad Mohammadi Aria,[†] Ugur Meric Dikbas,[‡] Sadra Sadeghi,[§] Baskaran Ganesh Kumar,[∥] Mehmet Sahin,[⊥] Ibrahim Halil Kavakli,[‡,#] Cleva W. Ow-Yang,[¶] and Sedat Nizamoglu*[,†,§,∥]

[†]Department of Biomedical Science and Engineering, Koç University, Istanbul 34450, Turkey
[‡]Department of Molecular Biology and Genetics, Koç University, Istanbul 34450, Turkey
[§]Department of Material Science and Engineering, Koç University, Istanbul 34450, Turkey
[∥]Department of Electrical and Electronics Engineering, Koç University, Istanbul 34450, Turkey
[⊥]Department of Materials Science and Nanotechnology Engineering, Abdullah Gul University, Kayseri 38080, Turkey
[#]Department of Chemical and Biological Engineering, Koç University, Istanbul 34450, Turkey
[¶]Department of Material Science and Nano Engineering, Sabanci University, Istanbul 34956, Turkey

Supporting Information

ABSTRACT: **Light-induced stimulation of neurons *via* photoactive surfaces offers rich opportunities for the development of therapeutic methods and high-resolution retinal prosthetic devices. Quantum dots serve as an attractive building block for such surfaces, as they can be easily functionalized to match the biocompatibility and charge transport requirements of cell stimulation. Although indium-based colloidal quantum dots with type-I band alignment have attracted significant attention as a nontoxic alternative to cadmium-based ones, little attention has been paid to their photovoltaic potential as type-II heterostructures. Herein, we demonstrate type-II indium phosphide/zinc oxide core/shell quantum dots that are incorporated into a photoelectrode structure for neural photostimulation. This induces a hyperpolarizing bioelectrical current that triggers the firing of a single neural cell at 4 μW mm^{-2}, 26-fold lower than the ocular safety limit for continuous exposure to visible light. These findings show that nanomaterials can induce a biocompatible and effective biological junction and can introduce a route in the use of quantum dots in photoelectrode architectures for artificial retinal prostheses.**

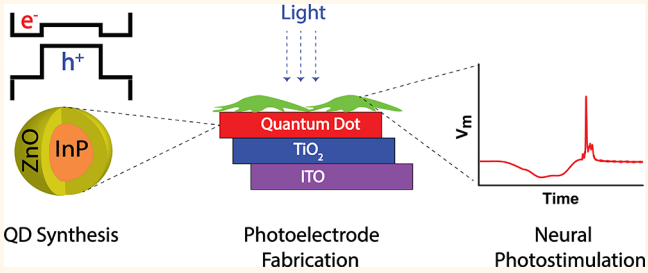

KEYWORDS: *quantum dot, indium phosphide, zinc oxide, type-II core/shell, neural, photostimulation, biocompatible*

Stimulation of the neural tissue and cells can treat a wide range of common and severe health problems, including hearing loss, chronic pain, incontinence, obesity, diabetes, and retinal degeneration.[1] Light offers an effective way of communication with such biological systems, and light-induced cell stimulation offers many opportunities from cell culture and neural network analysis *in vitro* to sensing and regulation *in vivo*.[2−5] Light-induced stimulation can be achieved either by genetic modification of the cellular membrane or by extracellular excitation *via* prosthetic devices and photoactive surfaces.[6−8] These photoactive layers have the advantages of high spatial resolution and simple fabrication combined with strong electrical stimulation of neurons, and nanomaterials offer adjustable compositional and electronic properties that can meet the needs of the biocompatibility and charge transport requirements of the neural interfaces.

Discovery of the quantum confinement effect in semiconductor quantum dots (QDs)[9−11] and introduction of chemical synthesis methods for them[12−15] have extended their application area in LEDs,[16−21] transistors,[22] detectors,[23] biological labeling,[24,25] bioassays[26,27] and *in vivo* imaging;[28] in addition, QDs also have significant potential in neural photostimulation due to their exceptional spectral sensitivity and stability.[29] Even though cadmium- and mercury-based QDs have been reported for neural interfaces,[30,31] indium phosphide (InP)-based quantum dots are accepted as a promising alternative due to their reduced toxicity[32−34] and tunable photoluminescence (PL) covering the blue to near-infrared.[35,36] Various materials were grown on the InP core as an outer shell (see the list in Table S1 in the Supporting Information) to suppress nonradiative losses in surface

Received: April 20, 2018
Accepted: July 18, 2018
Published: July 18, 2018

DOI: 10.1021/acsnano.8b02976
ACS Nano 2018, 12, 8104–8114

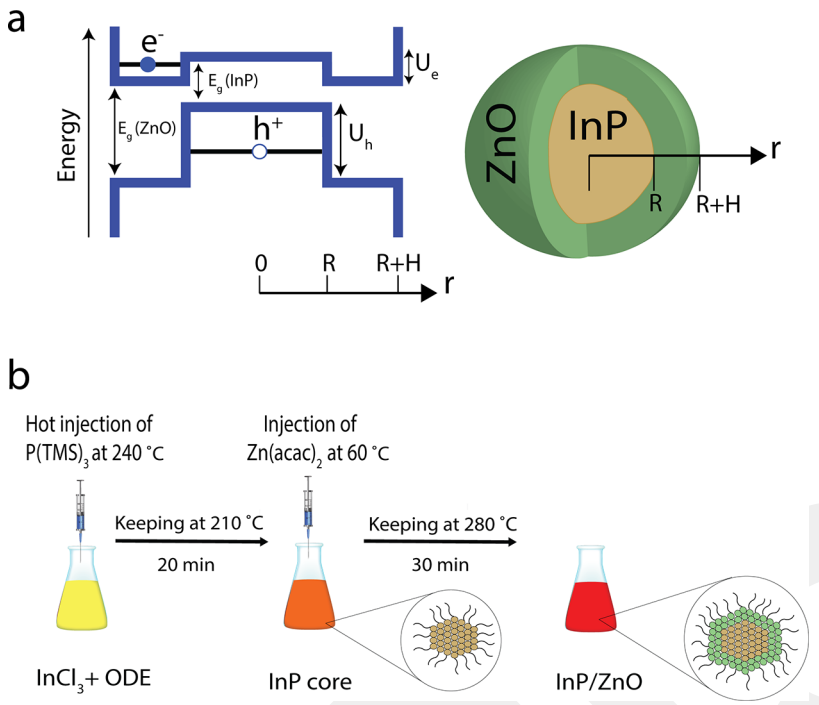

Figure 1. Electronic structure and synthesis procedure of the InP/ZnO core/shell quantum dots (QDs). (a) Band alignment (blue lines) and the lowest-energy electron and hole quantized levels (black lines) of the bulk InP/ZnO heterojunction and the representation of an InP/ZnO core/shell QD. [InP (VB = −3.73 eV, CB = −5.18 eV), ZnO (VB = −4.6 eV, CB = −8 eV).[45]] (b) Schematic representation of the synthesis procedure of InP core and InP/ZnO core/shell QDs.

trap states and confine both electrons and holes in the core to obtain narrower PL line widths and increased fluorescence quantum yield.[37−40]

Quantum dots with type-II band alignments, in which the charge carriers start to be delocalized from each other, provide benefits for optical gain,[41] photocurrent generation,[42] and emission wavelength tunability.[43] However, the reported type-II heterostructures generally include highly toxic cadmium content (see Table S2). Zinc oxide (ZnO) has the potential to form a type-II band alignment by incorporation onto an InP core as we reported previously (see Figure 1a).[44] ZnO is a wide band gap semiconductor (3.37 eV[45]), which has been used for gas sensors, varistors, generators of surface acoustic waves, and solar cells due to its optical, acoustic, and electric properties.[46−48] Advantageously, it has high radiation, chemical, and thermal resistance;[46] in addition, it shows higher biocompatibility compared to nonoxide materials and has been used for various biological applications.[49,50] Moreover, it can provide an oxidation-resistant protective and electron-transporting layer on the InP core. Previously, we demonstrated efficient luminescent solar concentrators (LSCs) based on these type-II QDs.[44] But, to the best of our knowledge, there is no previous report in the literature of biocompatible indium-based type-II QDs for neural interfaces.

In this study, we propose and demonstrate biocompatible indium-based QDs with type-II band alignment for neural interfaces. We describe the synthesis and characterization of the QDs, consisting of an InP core surrounded by a crystalline ZnO shell. Due to the photovoltaic and photoconduction potential of type-II heterostructures, the quantum dots are integrated into a photoelectrode structure, and the biocompatible material content of the electrode allowed the growth and differentiation of cells on it. Upon illumination, the photoelectrode generates an extracellular current that successfully hyperpolarizes the cell membrane and stimulates an action potential.

RESULTS AND DISCUSSION

Strategy for the Synthesis of InP/ZnO Core/Shell QDs. To grow thick and defect-free shells, a lower lattice mismatch across a heterojunction is desirable. Even though the lattice mismatch between InP and ZnO is 11%, which is higher than the well-known InP/ZnS lattice mismatch (∼8%),[51] a type-II heterostructure of CdTe/ZnSe with a higher lattice mismatch of up to 14% has already been reported that exhibits excellent optical and electronic properties.[52] Therefore, the lattice mismatch between InP and ZnO is at a level that can facilitate crystal growth. Moreover, the surface chemistry plays a critical role in the synthesis of QD heterostructures. Various reaction additives were reported in the literature to improve the quantum yield and broad size distribution of InP QDs, by addressing the affinity of InP for covalent binding and the oxidation sensitivity of the reactant precursors.[53] Among these methods, Nann provided a simple method to obtain highly luminescent InP cores using zinc carboxylates for surface passivation.[38] The addition of zinc carboxylates, such as zinc undecylenate, passivates surface dangling bonds and improves solubility of the InP core QDs. Hence, we selected the use of Nann's method for the initial growth of the InP core.

For growing the ZnO shell, we used the thermal decomposition of zinc acetylacetonate as we reported previously.[44] Thermal decomposition of zinc acetate ($Zn(OAc)_2$) and zinc acetylacetonate ($Zn(acac)_2$) has been reported in the literature for the synthesis of ZnO QDs.[44,54−58] To obtain smaller and more monodisperse ZnO QDs with weaker trap emission, $Zn(acac)_2$ was chosen as a zinc precursor.[58] Moreover, oleylamine (OAM) as stabilizing agent prevents ZnO grains from aggregating.[56] Briefly, InP cores were first synthesized by hot injection of tris(trimethylsilyl)phosphine ($P(TMS)_3$) on indium chloride ($InCl_3$) in the presence of OAM and oleic acid (OA) ligands with

DOI: 10.1021/acsnano.8b02976
ACS Nano 2018, 12, 8104−8114

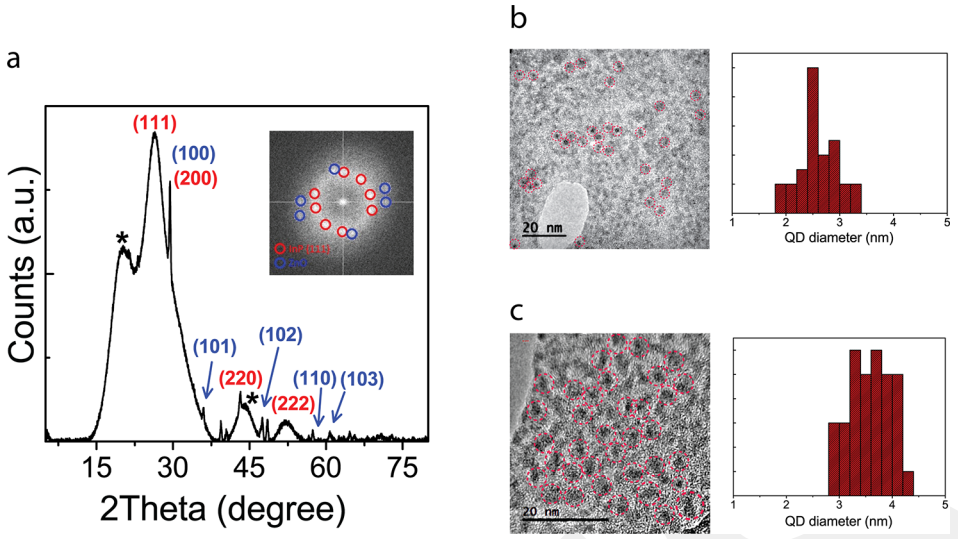

Figure 2. Structural analysis of the InP/ZnO core/shell quantum dots (QDs). (a) XRD pattern of the InP/ZnO core/shell QDs (inset: spatial frequencies in the FFT corresponding to HRTEM image components arising from the InP and ZnO crystallographic planes). Bright-field HRTEM image and particle size distribution of the (b) InP core and (c) InP/ZnO core/shell QDs on a single layer graphine oxide flake.

1-octadecene (ODE) as the solvent. After the core formation, the shell precursor, consisting of $Zn(acac)_2$, OAM, OA, and ODE, was added to the InP core solution. Thermal decomposition of $Zn(acac)_2$ occurred by heating the solution, which allowed the formation of a ZnO shell on the InP core (Figure 1b) (see the Methods section for the detailed synthesis procedure).

Structural Analysis. The final InP/ZnO heterostructure has cubic InP and hexagonal ZnO crystal structures according to the X-ray diffraction (XRD) pattern (Figure 2a). The major peaks correspond to the (111), (200), (220), and (222) crystalline planes of the cubic phase of InP (PDF 00-013-02-32). The three diffraction peaks of the hexagonal ZnO crystal structure (PDF 00-036-1451) are shown in the (100), (101), and (102) planes. The shoulders beside the (111) and (220) planes of InP, which are marked by a star, may be due to the impurities.[38,44] The narrow peaks reflect a high degree of crystallinity. All major peaks of the InP/ZnO heterostructure experience a shift toward higher angles, indicating a decreased average lattice parameter. It comes from the fact that the ZnO lattice constant (5.20 Å) is smaller than that of cubic InP (5.86 Å).

Bright-field high-resolution transmission electron microscope (HRTEM) images confirmed the size of the InP core (Figure 2b) and InP/ZnO (Figures 2c, S1) QDs to be 2.6 ± 0.34 and 3.58 ± 0.39 nm, respectively. To prove the existence of InP and ZnO crystal structures, we identified the spatial frequencies corresponding to crystalline planes contributing to the quantum dot images by fast Fourier transform (FFT) analysis performed on the HRTEM image (Figure 2a, inset). The spots of high spatial frequency in the FFT pattern were identified to be consistent with the (111) of InP (PDF 00-013-02-32) and the low-index planes of ZnO (PDF 00-036-1451) (Figure 1a, inset).

Quantum Mechanical Calculations and Optical Analysis. We analyzed the electronic properties of a single InP core and InP/ZnO core/shell QD structures by solving the Schrödinger and Poisson equations under the effective mass approximation and the BenDaniel−Duke boundary condition (details are provided in the Supporting Information). The band offsets in conduction and valence bands of InP/ZnO QD are determined as 0.100 and 2.12 eV, respectively, by means of the experimental affinity values. All material parameters used in the calculations are listed in Table S3 of the Supporting Information. The details of the calculations can be found elsewhere.[59] The initial InP core quantum dot shows a type-I alignment due to the high finite confinement potential model for the ligand and the solution environment. In this structure, both excited charges, the electron and hole, are confined in the same spatial region, which enables an attractive Coulomb potential between the electron and hole of 146 meV. In addition, the electron shows higher confinement energy (0.900 eV) in comparison with the hole (0.246 eV) due to the lower electron mass (Figure 3a). These features lead to an effective band gap energy between 1S electron and hole energy states corresponding to 470 nm, which is close to the kink of the experimentally measured absorption spectrum due to the lowest-energy 1S states (Figure 3c). After a ZnO shell layer is grown on top of the InP core, the structure starts to transition toward a type-II alignment. While the hole is confined in the InP core, the electron wave function is repelled toward the ZnO shell due to its lower conduction band ground state energy. Therefore, as the band alignment shifts to a type-II structure, the electron delocalizes across the entire quantum dot and the hole is strongly confined in the core, leading to a quasi-type-II behavior (Figure 3b). Thus, the electron confinement energy and the exciton binding energy significantly decrease to 0.472 eV and 115 meV, respectively, while the hole confinement energy increases to 0.286 eV. This is because the attractive Coulomb potential decreases with increasing the size of the structure. Thus, a total 75 ± 8 nm red-shift becomes apparent in the absorption and luminescence spectra (Figure 3c), while the heterostructure transforms from an InP core to an InP/ZnO core/shell structure. Moreover, the overlap of the wave functions becomes lower (0.68) in comparison with the type-I InP core quantum dot structure (0.96). Since the radiative lifetime is inversely affected by the wave function overlap integral, the measured average lifetime increases (Figure 3d). PL decays were fit by a two-exponential decay, and the average lifetime was calculated from an intensity-weighted mean.[60] Therefore, the transition from a type-I to a quasi-type-II wave function confinement is responsible for the red-shift and lifetime increase

DOI: 10.1021/acsnano.8b02976
ACS Nano 2018, 12, 8104−8114

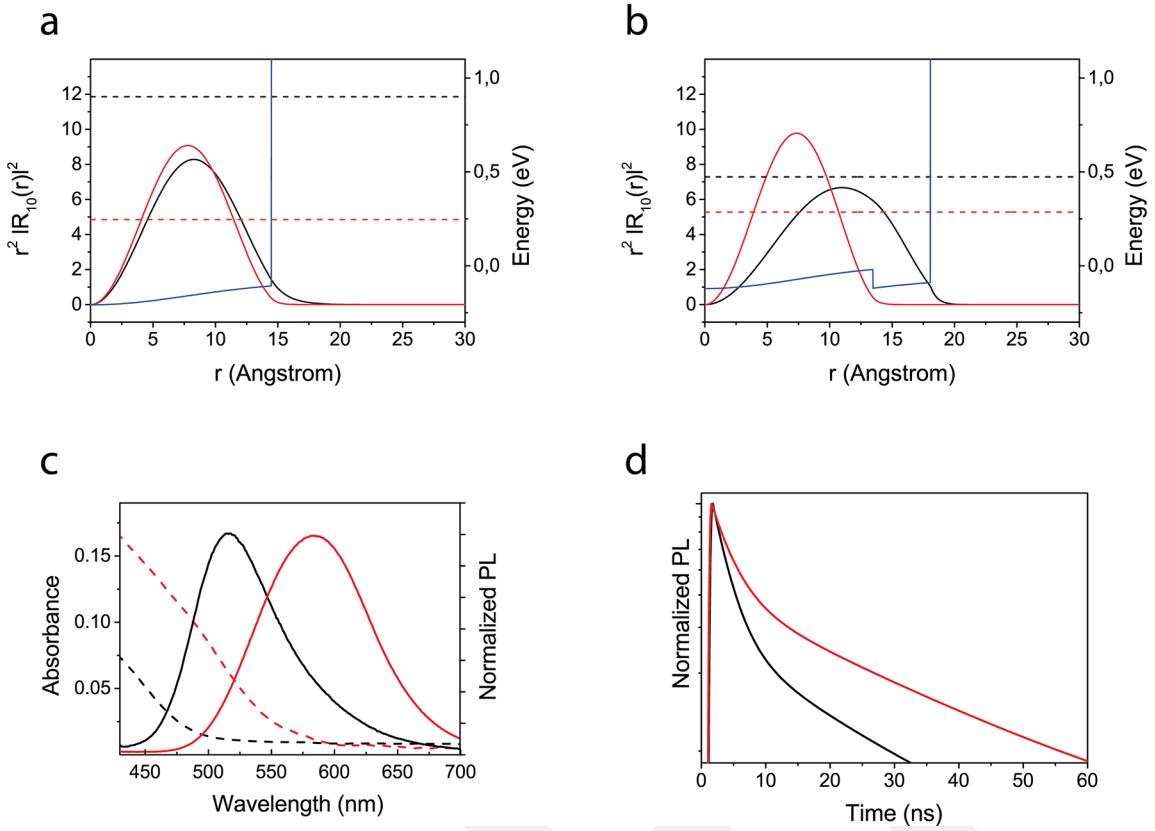

Figure 3. Quantum mechanical calculation and optical analysis of the InP/ZnO core/shell QDs. Electronic properties of (a) an InP core with type-I band alignment and (b) an InP/ZnO heterostructure with type-II band alignment determined by quantum mechanical calculations. In both figures (a) and (b), black lines correspond to the radial probability distribution of the electron, while red ones show a radial probability distribution of the holes. Dashed lines represent single electron and hole energies; blue line corresponds to confinement potential profile for the electron. To avoid confusion, only the conduction band profile in (a) and (b) are shown. (c) Steady-state absorbance (dashed) and photoluminescence (PL) (solid) of the InP core (black) and InP/ZnO core/shell QDs (red) dispersed in hexane. (d) Time-resolved PL of the InP core (black) and InP/ZnO core/shell QDs (red) dispersed in hexane.

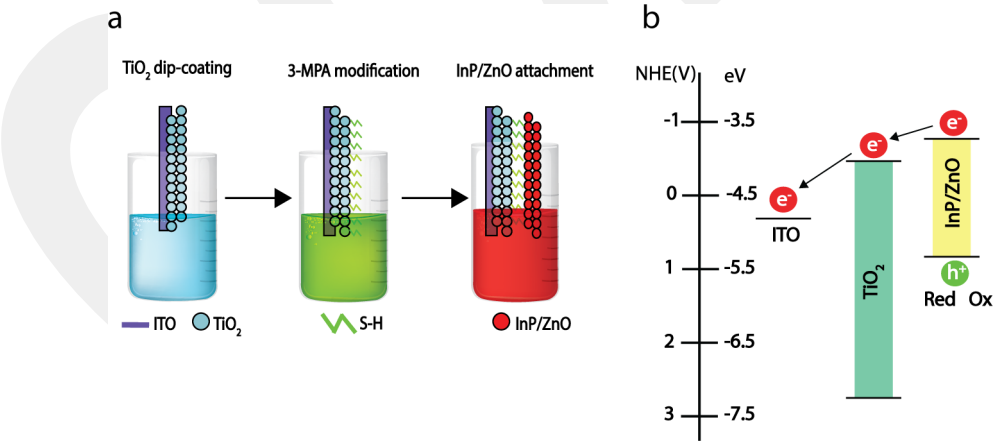

Figure 4. Photoelectrode fabrication. (a) Schematic illustration of the photoelectrode fabrication steps. (b) Band diagram of the InP/ZnO QD, TiO_2,[67] and ITO[68] (InP/ZnO QD energy levels were derived from the quantum mechanical calculations).

in the observed shift in the spectral and temporal luminescence characteristics. Moreover, ZnO shell growth passivates the InP core surface and enhances the quantum yield from 9.27 ± 1.7% (for the InP core) to 29.1 ± 2.8% (for InP/ZnO). The effect of the ZnO shell thickness on the QY was discussed in our previous study in detail.[44]

Photocurrent Measurement. Heterostructures with type-II band alignment are appropriate for charge disassociation and photocurrent generation. For such purposes, we prepared photoelectrodes by attaching the InP/ZnO QDs onto indium tin oxide (ITO) substrates with 3-mercaptopropionic acid (3-MPA)-modified titanium dioxide (TiO_2) nanoparticles (Figure 4a). 3-MPA is a bifunctional linker molecule, which has both carboxylate and thiol functional groups. It can facilitate binding between InP/ZnO QDs and a TiO_2 film,[61−63] and it can help monolayer coverage of the InP/ZnO film on the TiO_2 network.[64]

DOI: 10.1021/acsnano.8b02976
ACS Nano 2018, 12, 8104−8114

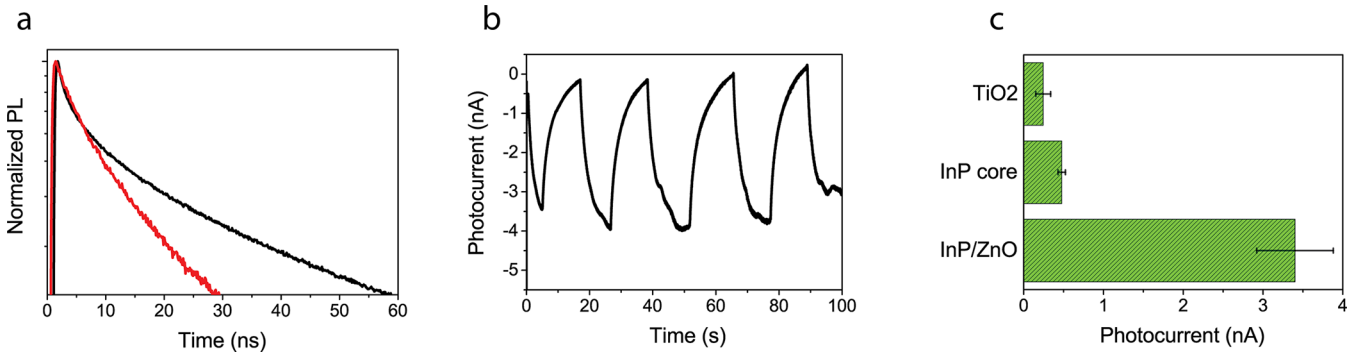

Figure 5. Photoelectrode characteristics. (a) Time-resolved PL of the InP/ZnO (black) and TiO_2−InP/ZnO (red) films. (b) Photocurrent response of the fabricated InP/ZnO-based photoelectrode under an illumination of 4 $\mu W/mm^2$. (c) Photocurrent measured for the bare TiO_2, InP core based photoelectrode, and InP/ZnO-based photoelectrode. The photocurrent of three different samples and three different points was measured to report average and error bar values.

Initially absorption generates electron−hole pairs in the InP/ZnO QDs. Since the linker is a short chain molecule (≈6 Å[65]), it positions the InP/ZnO and TiO_2 nanomaterials in close proximity and enables strong interparticle interaction. Because the difference between the two conduction band energy levels of TiO_2 (−0.5 V *versus* NHE[66]) and InP/ZnO (−0.8 V *versus* NHE[67]) leads to the coupling of an excited electron to an available state in TiO_2, the electron is expected to be transferred from InP/ZnO to TiO_2 and from TiO_2 to ITO (see Figure 4b). This result implies that the main contribution to the current originates from the photoinduced electron transfer.

The excited-state interaction of InP/ZnO QD, TiO_2, and oxygen in the environment leads to a speeding up of the time-resolved PL decay. The average lifetime of the InP/ZnO QD decreased after anchoring onto TiO_2 particles, validating the charge transfer to TiO_2 (Figure 5a).[64] We can estimate the charge-transfer rate constant using eq 1, which is around $4.01 \times 10^7\ s^{-1}$. Moreover, holes scavenged by the redox couple are also responsible for photocurrent generation.

$$k_{et} = \frac{1}{\tau(\mathrm{InP/ZnO} + \mathrm{TiO_2})} - \frac{1}{\tau(\mathrm{InP/ZnO})} \quad (1)$$

The photocurrent produced by the photoelectrode was measured with the electrophysiology system amplifier operated in voltage clamp mode. The photocurrent direction is from the photoelectrode toward the Ag/Cl wire of the pipet, indicative of a reduction process or electron uptake from the electrolyte by the photoanode.[67] A typical photocurrent response showed an ionic current of 3.40 ± 0.48 nA for InP/ZnO-based photoelectrode, generated with 4 $\mu W/mm^2$ input and 450 nm LED light power (Figure 5b). Under the same irradiation level, TiO_2 nanoparticles alone on the ITO substrate showed a photocurrent of 128 ± 30 pA, being approximately 1 order of magnitude lower than that of the photoelectrode. The InP core based photoelectrode shows a lower photocurrent response (476 ± 47 pA) compared with InP/ZnO (Figures 5c and S3). The slow photocurrent rise in Figure 5b is possibly due to slow hole scavenging. To show the lack of internal reactions/degradation in QDs during illumination, we illuminated the photoelectrodes (450 nm, 4 $\mu W/mm^2$) for 60 min, and the photoelectrode did not show any degradation.

Cell Viability and Cytotoxicity Assessment. To evaluate the feasibility of the InP/ZnO photoelectrode for neural interfacing, we first investigated the toxicity of the photoelectrode on Neuro2A cells. As shown in Figure 6a, the photoelectrode did not exhibit any toxic effect on the cells by measuring the mitochondrial activity with 3-(4,5-dimethylthiazol-2-yl)-2,5-diphenyltetrazolium bromide (MTT) under either dark or blue light conditions. We, then, investigated the effect of the photoelectrode on membrane integrity of the cells by a lactate dehydrogenase (LDH) assay. The membrane integrity of the cells grown on a photoelectrode and ITO control had a comparable amount of LDH activity in media at different time points, which suggested that the photoelectrode statistically did not have any effect on the membrane integrity (Figure 6b). Finally, the morphology of the cells grown on the photoelectrode and ITO control was examined by fluorescence microscopy. As can be seen in Figure 6c, the morphologies of the cells grown on the both the photoelectrode and ITO control were identical as assessed by DAPI and actin staining.

Neural Photostimulation. Anode break stimulation has been reported for heart and nerve cells, which originates from hyperpolarization-activated cation currents.[69−72] Injection of a long anodic pulse into the cell can cause this phenomenon. The hyperpolarization as a result of the anode current initiates an action potential by decreasing the potassium conductance, which leads to removing inactivation.[69,70] Equation 2 describes the time-dependent membrane,[72] in which V, V_K, V_{Na}, $V_{L,}$ C_M, g_K, g_{Na}, and g_L are membrane potential, potassium resting potential, sodium resting potential, leakage resting potential, membrane capacitance, potassium conductance, sodium conductance, and leakage conductance, respectively. All material parameters used in the calculations are listed in Table S4 of the Supporting Information.

$$\frac{dV}{dt} = -\frac{1}{C_M}\{\bar{g}_K n^4(V - V_K) + \bar{g}_{Na} m^3 h(V - V_{Na}) + \bar{g} l(V - V_l)\} \quad (2)$$

The probability functions of m, n, and h depend on the membrane potential and can be calculated from the activation and inactivation rate constants.

$$\frac{dm}{dt} = \alpha_m(V)(1 - m) - \beta_m(V)m$$
$$\frac{dn}{dt} = \alpha_n(V)(1 - n) - \beta_n(V)n$$
$$\frac{dh}{dt} = \alpha_h(V)(1 - h) - \beta_h(V)h$$

To explain the anode break excitation, we simulated the H−H model for a giant squid axon. Figure S4 shows the generated

DOI: 10.1021/acsnano.8b02976
ACS Nano 2018, 12, 8104−8114

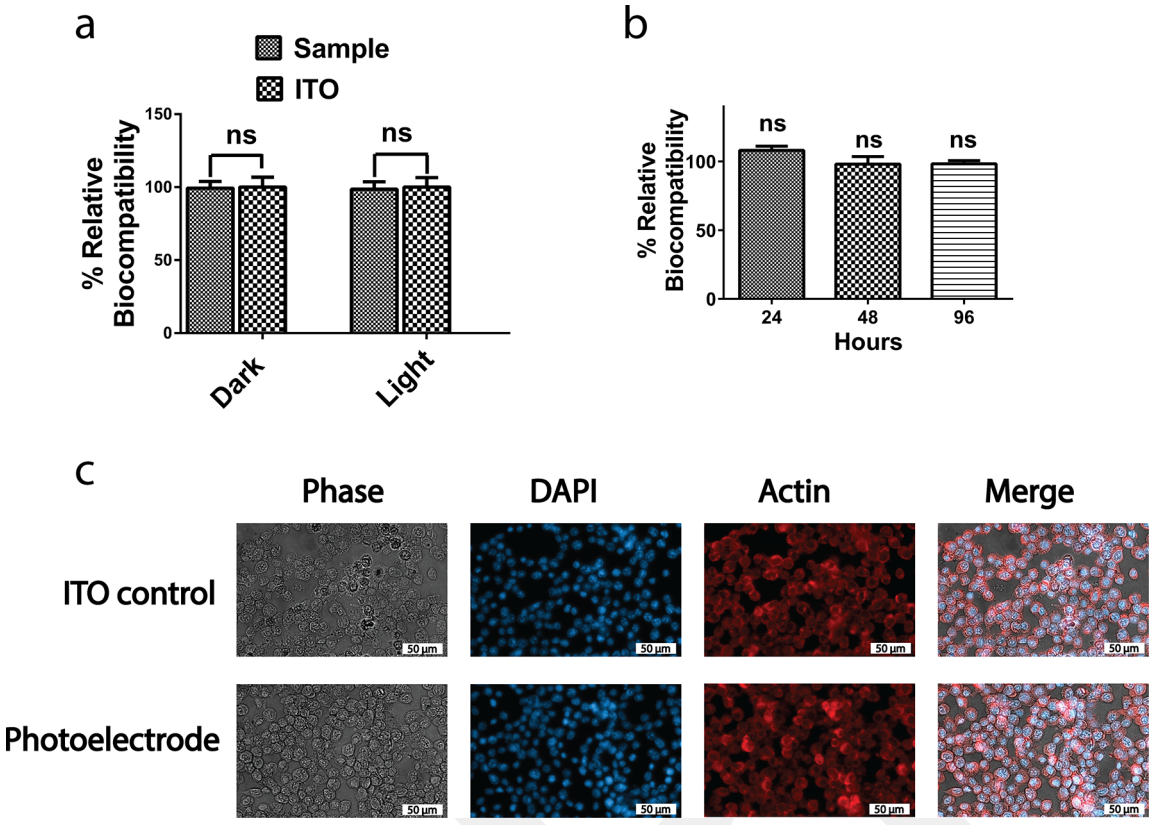

Figure 6. Cell viability and cytotoxicity assessment. The assessment of the photoelectrodes on (a) cell metabolic activity with MTT. Results are presented in a column bar graph plotting the mean with the standard error of the mean (SEM). An unpaired two-tailed *t* test was performed to determine the level of significance. (b) Cell membrane integrity with LDH assay. A one-sample *t* test was performed to check if the column means were statistically different than a hypothetical mean of 100%. Each experiment was carried out with at least three biological replicates. *$p < 0.05$ was considered as statistically significant, and nonsignificant differences are presented as "ns". (c) Effect of the photoelectrode on the cell morphology visualized by fluorescence microscopy after DAPI staining and actin immunolabeling (scale bar: 50 μm).

action potential as a result of anodic current. When the membrane potential is changed from a negative value toward zero, the activation function of *n* increases and the inactivation gate of *h* drastically drops (Figure S4a–d). The increase of the *n* parameter leads to both higher potassium current (Figure S4f) and a decrease of inactivation function of *h*, which subsequently causes an opening of sodium channels (and an increase of the sodium current in Figure S4e) and firing of an action potential.

We use the photoelectrode for neural photostimulation *via* the transduction of energy from photons to electrons. Figure 7a shows the setup used to measure the photostimulation of neurons: the electrophysiology system for cell membrane potential recording, the photoelectrode (InP/ZnO–TiO_2–ITO substrate) for photostimulation of the cells, and an LED light source for light illumination. PC12 cells were grown on the photoanode and differentiated *via* nerve growth factor (NGF) treatment, which has been reported before for differentiated PC12 cells on regular sterile plates.[73] Figure 7b and c show a single whole cell recording for measuring both excitability of cells and photostimulation investigation and action potential generation under the current clamp technique, respectively. The input current level of 350 pA was observed to be the threshold for firing an action potential, after sweeping different levels of injection currents. In a current clamp mode configuration, we studied the photostimulation effect on the membrane voltage. As introduced in the photocurrent discussion, the photocurrent is anodic, which needs to generate a negative potential on the membrane. Thus, a light pulse with an intensity of 4 μW/mm^2 enabled hyperpolarization of the membrane and fired a single neural cell. We repeated the hyperpolarization-induced photostimulation for $N = 4$, and the membrane hyperpolarization was found to be -45 ± 10 mV at 4 μW/mm^2. For example, a similar neural stimulation mechanism based on hyperpolarization has been already proposed and measured for retinal neural cells.[74,75] Since the hyperpolarization strength is directly proportional to the photocurrent level, the spectral regions that have lower absorption will generate lower photocurrent, and hence they require higher intensity levels to stimulate a neuron. Therefore, we measured the photocurrent response of the photoelectrode at different excitation colors. The maximum photocurrent can be observed under blue light in comparison with green and red excitation colors due to stronger absorption at shorter wavelengths. From this measurement, we expect that at 550 nm 3.5-fold and at 650 nm 30.5-fold higher light intensity are required (Figure S7).

Advantageously the light intensity of the photoanode that induces stimulation by a blue excitation is 26-fold lower than the ocular safety limit for continuous exposure to visible light (106.93 μW/mm^2), and it is also in the range of the daylight retinal irradiance (0.1–10 μW/mm^2).[76,77] The intensity level that generates an action potential is also significantly lower than the previous report, which uses quantum dots for neural photostimulation.[78] For example, HgTe (and CdTe) nanocrystal layers have been used to stimulate the neurons.[30,31] However,

DOI: 10.1021/acsnano.8b02976
ACS Nano 2018, 12, 8104–8114

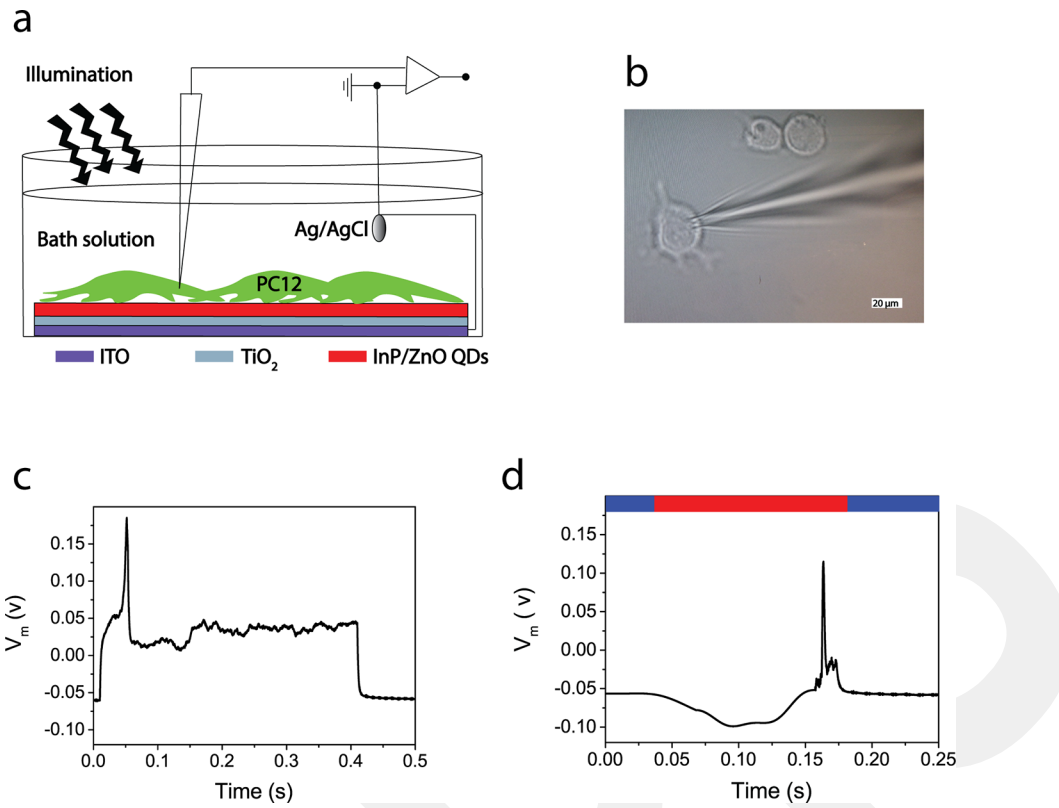

Figure 7. Neural photostimulation by the photoelectrode. (a) Schematic illustration of the neural photostimulation and recording setup. (b) Photograph of a patch-clamped PC12 cell. (c) Activation of a PC12 cell on the photoelectrode in current clamp mode in the dark. (d) Photostimulation of a PC12 cell on the photoelectrode under illumination. (Red bar: the time period under illumination of 4 μW/mm^2; blue bar: the time period in the dark.)

the cell stimulation by those films was observed from 2 to 8 mW/mm^2, which is approximately 18−75 times higher than the ocular safety limit for continuous exposure to visible light.[76] Herein, the light sensitivity for neurostimulation is enhanced due to the energy gradient between type-II quantum dots and the photoelectrode and due to improved photovoltaic property (electron−hole separation) of type-II quantum dots. In addition, the highly toxic cadmium and tellerium content of quantum dots in the previous reports may be adversely affecting the electronic coupling between the quantum dot layer and the cell. Moreover, no interfacial layer (*e.g.*, polylysine, poly(acrylic acid)/polylysine) is used to enhance the biocompatibility and promote cell attachment.[30] Hence, the biocompatibility of type-II InP/ZnO quantum dots in a photoelectrode structure facilitated a reliable and effective bionanojunction.

CONCLUSIONS

In conclusion, type-II InP/ZnO core/shell QDs were synthesized and used in a photoelectrode architecture for neural interfaces. The quantum dot structure of an InP core and ZnO shell was proved by crystallographic, structural, and optical analyses, supported by quantum mechanical simulations. We incorporated these QDs into a photoanode structure to build a photoactive surface, and neural cells were successfully grown and differentiated on the photoelectrode, with preservation of its optoelectronic functionality. The photoelectrode effectively hyperpolarizes the cell membrane and stimulates an action potential at an irradiance level lower than the ocular safety limit. Therefore, this study introduces biocompatible quantum dot based neural interfaces.

MATERIALS AND METHODS

Synthesis of the InP/ZnO QDs. *Chemicals.* Zinc undecylenate (99%), oleic acid (OA) (99%), oleylamine (OAM) (99%), 1-octadecene (ODE) (90%), indium chloride ($InCl_3$) (99%), Tris(trimethylsilyl)phosphine ($P(TMS)_3$) (95%), and zinc acetylacetonate hydrate ($Zn(acac)_2$) were purchased from Sigma-Aldrich. ODE was purified at 100 °C by evacuation and refilling with nitrogen for 1 h. All the procedures were performed in a nitrogen-filled glovebox with an O_2 level below 1 ppm using anhydrous solvents.

InP Core. First, 86 mg of zinc undecylenate, 44 mg of $InCl_3$, 64 μL of OA, and 133 μL of OAM were mixed with 6 mL of ODE (5 < pH < 6) and heated to 100 °C. The flask was evacuated and refilled with nitrogen to provide an oxygen- and water-free reaction atmosphere. Then, it was heated to 220 °C (10 °C/min), and 1 mL of phosphine stock solution ($P(TMS)_3$-ODE 0.2 mmol mL^{-1}) was swiftly injected to the solution. The solution was kept at 190 °C for 20 min and then cooled to room temperature.

InP/ZnO Core/Shell. For the preparation of a ZnO stock solution, 17 mg of $Zn(acac)_2$, 22 μL of OA, and 660 μL of OAM were mixed in 4 mL of ODE at 60 °C. Then, 800 μL of ZnO stock solution was added to the above InP solution at 60 °C. The solution was heated to 290 °C and stirred for 20 min. Finally, it was cooled to room temperature.

Purification and Storage. After adding 1:1 ethanol/acetone to the final QD solution, it was centrifuged at 9000 rpm for 15 min two times. The precipitated QDs were dispersed in hexane and kept at 5 °C.

Photoelectrode Preparation. *Chemicals.* Titanium(IV) isopropoxide (TTIP) (99%), 2-propanol (IPA), and hydrochloric acid fuming (HCl) (37%) were purchased from Merck, and 3-mercaptopropionic (≥99%) was purchased from Sigma-Aldrich.

TiO_2 Films. A sol−gel dip-coating method was used to prepare TiO_2 films as reported previously.[79] The preparation of TiO_2 sol is as follows: TTIP was dissolved in IPA and HCl with a molar ratio of

DOI: 10.1021/acsnano.8b02976
ACS Nano 2018, 12, 8104−8114

IPA:TTIP:HCl equal to 20:1:0.1 under magnetic stirring at 25 °C. The resulting sol was mixed and vigorously stirred for 6 h. The synthesized TiO_2 particles show a fully anatase crystal structure (Figure S2). A KSV NIMA dip-coater was used to coat TiO_2 on ITO slides (20 mm × 20 mm × 1.2 mm). The dipping and withdrawal speed were fixed at 150 mm min^{-1}. Finally, films were dried at 70 °C for 1 h and heat treated at 450 °C for 2 h.

InP/ZnO Attachment on the TiO_2. The TiO_2 films were immersed in a 1 M 3-MPA acetonitrile solution for 1 day, then rinsed thoroughly with acetonitrile and toluene before being transferred to the QD solution. Finally, they were left in the QD solution for 3 days to ensure saturated adsorption of the QD onto the TiO_2.

Biological Experiments. *Cell Growth.* PC12 Adh and Neuro2A cell lines were used in electrophysiology and biocompatibility experiments, respectively. Neuro2A cells were cultured in Dulbecco's modified Eagle's medium (DMEM, Gibco 21969-035) supplemented with 10% heat-inactivated fetal bovine serum (FBS, Gibco 10500), 1% L-glutamine (Gibco, 25030−081), and 1% penicillin−streptomycin (Gibco 15240-062). Cultures were maintained in a 37 °C, 5% CO_2, 85% humidified incubator. Every 2−3 days, cells were subcultured and supplied with fresh medium. PC12 Adh cells were cultured in RPMI 1640 (PAN Biotech, P04-16500) medium supplemented with 10% donor horse serum (PAN Biotech, P30-0701HI), 5% FBS, and 1% penicillin−streptomycin. Cells were plated in 100 mm polystyrene dishes and maintained at 37 °C in a 5% CO_2 incubator with 85% humidity. Cultures were passaged every 2−3 days with a subculture ratio of 1:3.

Cytotoxicity. Photoelectrodes were cut into square pieces with a size of 0.40 × 0.40 cm and then sterilized as follows before adding cells onto them: Substrates were first treated with 70% ethanol and then air-dried. Next, they were exposed to a UV-lamp for 30 min for surface sterilization. Sterilized substrates were placed in a sterile 96-well plate. Neuro2A cells were seeded into a 96-well plate (1×10^4 cells per well) and cultured in DMEM containing 10% FBS (100 μL) and incubated for 24 h (37 °C, 5% CO_2). These experiments were performed under total darkness and blue-light (450 nm blue LED, 500 $\mu W/cm^2$) conditions. To allow cell adherence, samples were incubated at 37 °C in a 5% CO_2 incubator for 48 h. Then the growth medium was replaced with DMEM containing 1 mg/mL MTT solution to each well and further incubated for 4 h at 37 °C. Subsequently, the MTT media was removed and EtOH/DMSO (200 μL) was added to each well. The optical density (OD) was measured at 600 nm with a microplate reader (BioTek). The relative cell viability was calculated as follows: viability = $(OD_{sample}/OD_{control}) \times 100$. The OD_{sample} was obtained from the cells grown on a photoelectrode, and the $OD_{control}$ was obtained from the cells grown on the ITO substrate.

LDH Leakage Assay. To assess the membrane integrity of the Neuro2A cells in the presence and absence of the photoelectrode, an LDH leakage assay (CytoSelect LDH cytotoxicity assay kit, CBA-241, Cell Biolabs) was performed. Photoelectrodes were sterilized as described in the cytotoxicity method. ITO substrates with dH_2O and with 1% Triton X-100 were used as positive and negative controls throughout all experiments, respectively. After sterilization of the substrates, they were placed in 96-well plates, and 1.6×10^4 cells were seeded to each well. An LDH leakage assay was carried out as described in the product manual. Briefly, plates were incubated at 37 °C in a time-dependent manner (for 24, 48, and 96 h). After adding 1% Triton X-100 into negative control wells, 90 μL of all samples was transferred into a new plate. Next, 10 μL of LDH cytotoxicity assay reagent was added to each well. Plates were incubated at 37 °C and 5% CO_2 for 30 min. The presence of the LDH in media was measured at 450 nm by a Synergy H1 microplate reader (BioTek). All experiments were repeated as at least three biological replicates, and each biological replicate was carried out with three technical triplicates.

Immunolabeling and Fluorescence Microscopy. Neuro2A cells were grown on photoelectrodes and ITO control substrates. After 48 h, samples were fixed with methanol and washed three times with PBS. Cells were blocked in PBS solution containing 3% bovine serum albumin and 0.1% Triton X-100. Samples were incubated with mouse anti-actin primary antibody and washed three times with PBS. Finally, to visualize the nucleus and actin cytoskeleton of Neuro2A cells, DAPI and Alexa Fluor 488-conjugated anti-mouse secondary antibody was added respectively and washed with PBS before mounting. Substrates were mounted by Mowiol and imaged on a flouresence microscope (Zeiss-ObserverZ1) using Zen 2 blue edition software (Zeiss).

Instrumentation. *XRD.* Multiple layers of QD solution were drop-cast on a glass substrate, left to dry, and analyzed in a Bruker D2 Phaser X-ray diffractometer with Cu Kα radiation (λ = 1.541 Å).

TEM. Transmission electron microscopy (TEM) analysis was performed using a JEOL JEM-ARM200CFEG UHR microscope with a spherical aberration-corrected probe and equipped with a Gatan Orius SC200D CCD camera. Bright-field images were collected using an accelerating voltage of 200 keV. Specimens for TEM analysis were prepared by first placing a 10 μL droplet of aqueous suspension of single-layer graphene oxide (CheapTubes.com) onto a holey carbon film on a copper support grid, followed by deposition of a 10 μL droplet of ∼1 mM solution of nanocrystals in hexane.

Absorbance and PL. Absorbance spectra of the QDs were measured using a Shimadzu UV-3600 UV−vis−NIR spectrophotometer at 2 nm in the range of 400−700 nm. The steady-state PL analysis was done with a FluoroMax-3 spectrofluorimeter (Jobin Yvon Horiba) with a 2 nm slit in the same range of absorbance at 375 nm excitation wavelength.

Time-Resolved PL. Fluorescence decay was taken with a PicoQuant MicroTime 100 time-resolved confocal fluorescence microscope. The excitation beam was provided by 8 mW picosecond diode laser heads operating at 375 nm pulsed at a 20 MHz repetition rate.

Photocurrent Measurement. The photocurrent produced by the photoanode was measured with an electrophysiology system amplifier operated in voltage clamp mode with a patch pipet positioned closer than 1 μm to the electrode surface, a blue LED (450 nm, 4 $\mu W/mm^2$) served as a pulsed illumination source (LED's spectrum in Figure S5), and artificial cerebrospinal fluid was used as electrolytic solution, which has around 80% transmittance in the visible range (Figure S6). The photocurrent of three different samples and three different points was measured to report average and error bar values.

Electrophysiology Test. An EPC800 system made by HEKA was used for electrophysiology experiments. Whole patch clamp recordings were used for the PC12 cell membrane voltage and currents under GΩ seal condition with capillary pipets (8−10 MΩ) at room temperature. Capillary pulled glass electrodes contained a standard internal solution of 140 mM NaCl, 10 mM KCl, 5 mM $MgCl_2$, 10 mM HEPES, 0.5 mM EGTA, and 0.5 mM ATP, with pH adjusted using KOH to 7.2. The standard external solution contained 128 mM NaCl, 5 mM KCl, 1 mM $MgCl_2$, and 2.5 mM $CaCl_2$, and the pH was adjusted to 7.4 with NaOH. The same blue LED (450 nm, 4 $\mu W/mm^2$) was used as pulsed illumination source (LED's spectrum in Figure S5).

ASSOCIATED CONTENT

Supporting Information

The Supporting Information is available free of charge on the ACS Publications website at DOI: 10.1021/acsnano.8b02976.

Additional information (PDF)

AUTHOR INFORMATION

Corresponding Author

*E-mail: snizamoglu@ku.edu.tr.

ORCID

Houman Bahmani Jalali: 0000-0001-7212-9098
Sadra Sadeghi: 0000-0002-8569-1626
Baskaran Ganesh Kumar: 0000-0003-4705-499X
Mehmet Sahin: 0000-0002-9419-1711
Cleva W. Ow-Yang: 0000-0002-2909-0957
Sedat Nizamoglu: 0000-0003-0394-5790

DOI: 10.1021/acsnano.8b02976
ACS Nano 2018, 12, 8104−8114

Notes

The authors declare no competing financial interest.

ACKNOWLEDGMENTS

This project has received funding from the European Research Council (ERC) under the European Union's Horizon 2020 Research and Innovation Programme (grant agreement no. 639846). We thank KUYTAM (Koç University Surface Science and Technology Center) for providing XRD and UV−vis−NIR spectrophotometer infrastructures. We also thank Dr. Ceren Yilmaz Akkaya for XRD and Prof. Havva Funda Acar Yagci for the PL measurement.

REFERENCES

(1) Kotov, N. A.; Winter, J. O.; Clements, I. P.; Jan, E.; Timko, B. P.; Campidelli, S.; Pathak, S.; Mazzatenta, A.; Lieber, C. M.; Prato, M. Nanomaterials for Neural Interfaces. *Adv. Mater.* **2009**, *21*, 3970−4004.

(2) Gradinaru, V.; Thompson, K. R.; Zhang, F.; Mogri, M.; Kay, K.; Schneider, M. B.; Deisseroth, K. Targeting and Readout Strategies for Fast Optical Neural Control *in Vitro* and *in Vivo*. *J. Neurosci.* **2007**, *27*, 14231−14238.

(3) Levitz, J.; Pantoja, C.; Gaub, B.; Janovjak, H.; Reiner, A.; Hoagland, A.; Schoppik, D.; Kane, B.; Stawski, P.; Schier, A. F. Optical Control of Metabotropic Glutamate Receptors. *Nat. Neurosci.* **2013**, *16*, 507−516.

(4) Zrenner, E.; Bartz-Schmidt, K. U.; Benav, H.; Besch, D.; Bruckmann, A.; Gabel, V.-P.; Gekeler, F.; Greppmaier, U.; Harscher, A.; Kibbel, S. Subretinal Electronic Chips Allow Blind Patients to Read Letters and Combine Them to Words. *Proc. R. Soc. London, Ser. B* **2011**, *278*, 1489−1497.

(5) Choi, M.; Choi, J. W.; Kim, S.; Nizamoglu, S.; Hahn, S. K.; Yun, S. H. Light-guiding Hydrogels for Cell-based Sensing and Optogenetic Synthesis. *Nat. Photonics* **2013**, *7*, 987−994.

(6) Yizhar, O.; Fenno, L. E.; Davidson, T. J.; Mogri, M.; Deisseroth, K. Optogenetics in Neural Systems. *Neuron* **2011**, *71*, 9−34.

(7) Mathieson, K.; Loudin, J.; Goetz, G.; Huie, P.; Wang, L.; Kamins, T. I.; Galambos, L.; Smith, R.; Harris, J. S.; Sher, A. Photovoltaic Retinal Prosthesis with High Pixel Density. *Nat. Photonics* **2012**, *6*, 391−397.

(8) Maya-Vetencourt, J. F.; Ghezzi, D.; Antognazza, M. R.; Colombo, E.; Mete, M.; Feyen, P.; Desii, A.; Buschiazzo, A.; Di Paolo, M.; Di Marco, S. A Fully Organic Retinal Prosthesis Restores Vision in a Rat Model of Degenerative Blindness. *Nat. Mater.* **2017**, *16*, 681−689.

(9) Ekimov, A. I.; Onushchenko, A. A. Quantum Size Effect in Three-dimensional Microscopic Semiconductor Crystals. *JETP Lett.* **1981**, *34*, 363−366.

(10) Efros, A. L.; Efros, A. L. Interband Absorption of Light in a Semiconductor Sphere. *Semiconductors* **1982**, *16*, 772−775.

(11) Brus, L. A Simple Model for the Ionization Potential, Electron Affinity, and Aqueous Redox Potentials of Small Semiconductor Crystallites. *J. Chem. Phys.* **1983**, *79*, 5566−5571.

(12) Murray, C.; Norris, D. J.; Bawendi, M. G. Synthesis and Characterization of Nearly Monodisperse CdE (E= Sulfur, Selenium, Tellurium) Semiconductor Nanocrystallites. *J. Am. Chem. Soc.* **1993**, *115*, 8706−8715.

(13) Hines, M. A.; Guyot-Sionnest, P. Synthesis and Characterization of Strongly Luminescing ZnS-capped CdSe Nanocrystals. *J. Phys. Chem.* **1996**, *100*, 468−471.

(14) Dabbousi, B. O.; Rodriguez-Viejo, J.; Mikulec, F. V.; Heine, J. R.; Mattoussi, H.; Ober, R.; Jensen, K. F.; Bawendi, M. G. CdSe) ZnS Core-shell Quantum Dots: Synthesis and Characterization of a Size Series of Highly Luminescent Nanocrystallites. *J. Phys. Chem. B* **1997**, *101*, 9463−9475.

(15) Peng, X.; Schlamp, M. C.; Kadavanich, A. V.; Alivisatos, A. P. Epitaxial Growth of Highly Luminescent CdSe/CdS Core/shell Nanocrystals with Photostability and Electronic Accessibility. *J. Am. Chem. Soc.* **1997**, *119*, 7019−7029.

(16) Coe, S.; Woo, W.-K.; Bawendi, M.; Bulović, V. Electroluminescence from Single Monolayers of Nanocrystals in Molecular Organic Devices. *Nature* **2002**, *420*, 800−803.

(17) Sun, Q.; Wang, Y. A.; Li, L. S.; Wang, D.; Zhu, T.; Xu, J.; Yang, C.; Li, Y. Bright, Multicoloured Light-emitting Diodes Based on Quantum Dots. *Nat. Photonics* **2007**, *1*, 717−722.

(18) Caruge, J.; Halpert, J.; Wood, V.; Bulović, V.; Bawendi, M. Colloidal Quantum-dot Light-emitting Diodes with Metal-oxide Charge Transport Layers. *Nat. Photonics* **2008**, *2*, 247−250.

(19) Kim, T.-H.; Cho, K.-S.; Lee, E. K.; Lee, S. J.; Chae, J.; Kim, J. W.; Kim, D. H.; Kwon, J.-Y.; Amaratunga, G.; Lee, S. Y. Full-colour Quantum Dot Displays Fabricated by Transfer Printing. *Nat. Photonics* **2011**, *5*, 176−182.

(20) Qian, L.; Zheng, Y.; Xue, J.; Holloway, P. H. Stable and Efficient Quantum-dot Light-emitting Diodes Based on Solution-processed Multilayer Structures. *Nat. Photonics* **2011**, *5*, 543−548.

(21) Kumar, B. G.; Sadeghi, S.; Melikov, R.; Mohammadi Aria, M.; Bahmani Jalali, H.; Ow-Yang, C. W.; Nizamoglu, S. Structural Control of InP/ZnS Core/shell Quantum Dots Enables High-quality White LEDs. *Nanotechnology* **2018**, *29*, 345605.

(22) Konstantatos, G.; Badioli, M.; Gaudreau, L.; Osmond, J.; Bernechea, M.; de Arquer, F. P. G.; Gatti, F.; Koppens, F. H. Hybrid Graphene-quantum Dot Phototransistors with Ultrahigh Gain. *Nat. Nanotechnol.* **2012**, *7*, 363−368.

(23) McDonald, S. A.; Konstantatos, G.; Zhang, S.; Cyr, P. W.; Klem, E. J.; Levina, L.; Sargent, E. H. Solution-processed PbS Quantum Dot Infrared Photodetectors and Photovoltaics. *Nat. Mater.* **2005**, *4*, 138−142.

(24) Chan, W. C.; Nie, S. Quantum Dot Bioconjugates for Ultrasensitive Nonisotopic Detection. *Science* **1998**, *281*, 2016−2018.

(25) Bruchez, M.; Moronne, M.; Gin, P.; Weiss, S.; Alivisatos, A. P. Semiconductor Nanocrystals as Fluorescent Biological Labels. *Science* **1998**, *281*, 2013−2016.

(26) Clapp, A. R.; Medintz, I. L.; Mauro, J. M.; Fisher, B. R.; Bawendi, M. G.; Mattoussi, H. Fluorescence Resonance Energy Transfer Between Quantum Dot Donors and Dye-labeled Protein Acceptors. *J. Am. Chem. Soc.* **2004**, *126*, 301−310.

(27) Goldman, E. R.; Clapp, A. R.; Anderson, G. P.; Uyeda, H. T.; Mauro, J. M.; Medintz, I. L.; Mattoussi, H. Multiplexed Toxin Analysis Using Four Colors of Quantum Dot Fluororeagents. *Anal. Chem.* **2004**, *76*, 684−688.

(28) Michalet, X.; Pinaud, F.; Bentolila, L.; Tsay, J.; Doose, S.; Li, J.; Sundaresan, G.; Wu, A.; Gambhir, S.; Weiss, S. Quantum Dots for Live Cells, *in Vivo* Imaging, and Diagnostics. *Science* **2005**, *307*, 538−544.

(29) Bareket-Keren, L.; Hanein, Y. Novel Interfaces for Light Directed Neuronal Stimulation: Advances and Challenges. *Int. J. Nanomed.* **2014**, *9*, 65−83.

(30) Pappas, T. C.; Wickramanyake, W. S.; Jan, E.; Motamedi, M.; Brodwick, M.; Kotov, N. A. Nanoscale Engineering of a Cellular Interface with Semiconductor Nanoparticle Films for Photoelectric Stimulation of Neurons. *Nano Lett.* **2007**, *7*, 513−519.

(31) Lugo, K.; Miao, X.; Rieke, F.; Lin, L. Y. Remote Switching of Cellular Activity and Cell Signaling Using Light in Conjunction with Quantum Dots. *Biomed. Opt. Express* **2012**, *3*, 447−454.

(32) Lin, G.; Ouyang, Q.; Hu, R.; Ding, Z.; Tian, J.; Yin, F.; Xu, G.; Chen, Q.; Wang, X.; Yong, K.-T. *In Vivo* Toxicity Assessment of Non-cadmium Quantum Dots in BALB/c Mice. *Nanomedicine* **2015**, *11*, 341−350.

(33) Brunetti, V.; Chibli, H.; Fiammengo, R.; Galeone, A.; Malvindi, M. A.; Vecchio, G.; Cingolani, R.; Nadeau, J. L.; Pompa, P. P. InP/ZnS as a Safer Alternative to CdSe/ZnS Core/shell Quantum Dots: *In Vitro* and *in Vivo* Toxicity Assessment. *Nanoscale* **2013**, *5*, 307−317.

(34) Chibli, H.; Carlini, L.; Park, S.; Dimitrijevic, N. M.; Nadeau, J. L. Cytotoxicity of InP/ZnS Quantum Dots Related to Reactive Oxygen Species Generation. *Nanoscale* **2011**, *3*, 2552−2559.

DOI: 10.1021/acsnano.8b02976
ACS Nano 2018, 12, 8104−8114

(35) Green, M. Solution Routes to III−V Semiconductor Quantum Dots. *Curr. Opin. Solid State Mater. Sci.* **2002**, *6*, 355−363.
(36) Xie, R.; Battaglia, D.; Peng, X. Colloidal InP Nanocrystals as Efficient Emitters Covering Blue to Near-infrared. *J. Am. Chem. Soc.* **2007**, *129*, 15432−15433.
(37) Xu, S.; Klama, F.; Ueckermann, H.; Hoogewerff, J.; Clayden, N.; Nann, T. Optical and Surface Characterisation of Capping Ligands in the Preparation of InP/ZnS Quantum Dots. *Sci. Adv. Mater.* **2009**, *1*, 125−137.
(38) Xu, S.; Ziegler, J.; Nann, T. Rapid Synthesis of Highly Luminescent InP and InP/ZnS Nanocrystals. *J. Mater. Chem.* **2008**, *18*, 2653−2656.
(39) Haubold, S.; Haase, M.; Kornowski, A.; Weller, H. Strongly Luminescent InP/ZnS Core−Shell Nanoparticles. *ChemPhysChem* **2001**, *2*, 331−334.
(40) Ippen, C.; Greco, T.; Wedel, A. InP/ZnSe/ZnS: A Novel Multishell System for InP Quantum Dots for Improved Luminescence Efficiency and Its Application in a Light-emitting Device. *J. Inf. Disp.* **2012**, *13*, 91−95.
(41) Klimov, V. I.; Ivanov, S. A.; Nanda, J.; Achermann, M.; Bezel, I.; McGuire, J. A.; Piryatinski, A. Single-exciton Optical Gain in Semiconductor Nanocrystals. *Nature* **2007**, *447*, 441−446.
(42) Gur, I.; Fromer, N. A.; Geier, M. L.; Alivisatos, A. P. Air-stable All-inorganic Nanocrystal Solar Cells Processed from Solution. *Science* **2005**, *310*, 462−465.
(43) Kim, S.; Lim, Y. T.; Soltesz, E. G.; De Grand, A. M.; Lee, J.; Nakayama, A.; Parker, J. A.; Mihaljevic, T.; Laurence, R. G.; Dor, D. M. Near-infrared Fluorescent Type II Quantum Dots for Sentinel Lymph Node Mapping. *Nat. Biotechnol.* **2004**, *22*, 93−97.
(44) Sadeghi, S.; Bahmani Jalali, H.; Melikov, R.; Ganesh Kumar, B.; Mohammadi Aria, M.; Ow-Yang, C. W.; Nizamoglu, S. Stokes-Shift-Engineered Indium Phosphide Quantum Dots for Efficient Luminescent Solar Concentrators. *ACS Appl. Mater. Interfaces* **2018**, *10*, 12975−12982.
(45) Van de Walle, C. G.; Neugebauer, J. Universal Alignment of Hydrogen Levels in Semiconductors, Insulators and Solutions. *Nature* **2003**, *423*, 626−628.
(46) Nickel, N. H.; Terukov, E. *Zinc Oxide-A Material for Micro-and Optoelectronic Applications: Proceedings of the NATO Advanced Research Workshop on Zinc Oxide as a Material for Micro-and Optoelectronic Applications*, St. Petersburg, Russia, June 23 to 25, 2004; Springer Science & Business Media, 2006; Vol. *194*.
(47) Rodnyi, P.; Khodyuk, I. Optical and Luminescence Properties of Zinc Oxide (Review). *Opt. Spectrosc.* **2011**, *111*, 776−785.
(48) Sun, Y.; Seo, J. H.; Takacs, C. J.; Seifter, J.; Heeger, A. J. Inverted Polymer Solar Cells Integrated with a Low-temperature-annealed Sol-gel-derived ZnO Film as an Electron Transport Layer. *Adv. Mater.* **2011**, *23*, 1679−1683.
(49) Rasmussen, J. W.; Martinez, E.; Louka, P.; Wingett, D. G. Zinc oxide Nanoparticles for Selective Destruction of Tumor Cells and Potential for Drug Delivery Applications. *Expert Opin. Drug Delivery* **2010**, *7*, 1063−1077.
(50) Wang, Y.; Wu, Y.; Quadri, F.; Prox, J. D.; Guo, L. Cytotoxicity of ZnO Nanowire Arrays on Excitable Cells. *Nanomaterials* **2017**, *7*, 80.
(51) Ramasamy, P.; Kim, B.; Lee, M.-S.; Lee, J.-S. Beneficial Effects of Water in the Colloidal Synthesis of InP/ZnS Core−shell Quantum Dots for Optoelectronic Applications. *Nanoscale* **2016**, *8*, 17159−17168.
(52) Smith, A. M.; Mohs, A. M.; Nie, S. Tuning the Optical and Electronic Properties of Colloidal Nanocrystals by Lattice Strain. *Nat. Nanotechnol.* **2009**, *4*, 56−63.
(53) Tamang, S.; Lincheneau, C.; Hermans, Y.; Jeong, S.; Reiss, P. Chemistry of InP Nanocrystal Syntheses. *Chem. Mater.* **2016**, *28*, 2491−2506.
(54) Du, Y.-P.; Zhang, Y.-W.; Sun, L.-D.; Yan, C.-H. Efficient Energy Transfer in Monodisperse Eu-doped ZnO Nanocrystals Synthesized from Metal Acetylacetonates in High-boiling Solvents. *J. Phys. Chem. C* **2008**, *112*, 12234−12241.
(55) Salavati-Niasari, M.; Davar, F.; Mazaheri, M. Preparation of ZnO Nanoparticles from [bis (acetylacetonato) zinc (II)]−oleylamine Complex by Thermal Decomposition. *Mater. Lett.* **2008**, *62*, 1890−1892.
(56) Liu, J.; Bei, Y.; Wu, H.; Shen, D.; Gong, J.; Li, X.; Wang, Y.; Jiang, N.; Jiang, J. Synthesis of Relatively Monodisperse ZnO Nanocrystals from a Precursor Zinc 2, 4-pentanedionate. *Mater. Lett.* **2007**, *61*, 2837−2840.
(57) Musić, S.; Šarić, A.; Popović, S. Formation of Nanosize ZnO Particles by Thermal Decomposition of Zinc Acetylacetonate Monohydrate. *Ceram. Int.* **2010**, *36*, 1117−1123.
(58) Nguyen, T.-L.; Michael, M.; Mulvaney, P. Synthesis of Highly Crystalline CdSe@ ZnO Nanocrystals *via* Monolayer-by-monolayer Epitaxial Shell Deposition. *Chem. Mater.* **2014**, *26*, 4274−4279.
(59) Şahin, M.; Nizamoglu, S.; Kavruk, A. E.; Demir, H. V. Self-consistent Computation of Electronic and Optical Properties of a Single Exciton in a Spherical Quantum Dot *via* Matrix Diagonalization Method. *J. Appl. Phys.* **2009**, *106*, 043704.
(60) Bahmani Jalali, H.; Melikov, R.; Sadeghi, S.; Nizamoglu, S. Excitonic Energy Transfer within InP/ZnS Quantum Dot Langmuir−Blodgett Assemblies. *J. Phys. Chem. C* **2018**, *122*, 11616−11622.
(61) Kamat, P. V. Quantum Dot Solar Cells. Semiconductor Nanocrystals as Light Harvesters. *J. Phys. Chem. C* **2008**, *112*, 18737−18753.
(62) Natan, M. J.; Thackeray, J. W.; Wrighton, M. S. Interaction of Thiols with N-type Cadmium Sulfide and N-type Cadmium Selenide in Aqueous Solutions: Adsorption of Thiolate Anion and Efficient Photoelectrochemical Oxidation to Disulfides. *J. Phys. Chem.* **1986**, *90*, 4089−4098.
(63) Lawless, D.; Kapoor, S.; Meisel, D. Bifunctional Capping of CdS Nanoparticles and Bridging to TiO_2. *J. Phys. Chem.* **1995**, *99*, 10329.
(64) Kongkanand, A.; Tvrdy, K.; Takechi, K.; Kuno, M.; Kamat, P. V. Quantum Dot Solar Cells. Tuning Photoresponse through Size and Shape Control of CdSe− TiO_2 Architecture. *J. Am. Chem. Soc.* **2008**, *130*, 4007−4015.
(65) Narayanan, S. S.; Sinha, S. S.; Verma, P. K.; Pal, S. K. Ultrafast Energy Transfer from 3-mercaptopropionic Acid-capped CdSe/ZnS QDs to Dye-labelled DNA. *Chem. Phys. Lett.* **2008**, *463*, 160−165.
(66) Grätzel, M. Photoelectrochemical Cells. *Nature* **2001**, *414*, 338−344.
(67) Zaban, A.; Mićić, O.; Gregg, B.; Nozik, A. Photosensitization of Nanoporous TiO_2 Electrodes with InP Quantum Dots. *Langmuir* **1998**, *14*, 3153−3156.
(68) Liu, D.; Kelly, T. L. Perovskite Solar Cells with a Planar Heterojunction Structure Prepared using Room-temperature Solution Processing Techniques. *Nat. Photonics* **2014**, *8*, 133−138.
(69) Robinson, R. B.; Siegelbaum, S. A. Hyperpolarization-activated Cation Currents: From Molecules to Physiological Function. *Annu. Rev. Physiol.* **2003**, *65*, 453−480.
(70) Ranjan, R.; Chiamvimonvat, N.; Thakor, N. V.; Tomaselli, G. F.; Marban, E. Mechanism of Anode Break Stimulation in the Heart. *Biophys. J.* **1998**, *74*, 1850−1863.
(71) Horch, K. W. *Neuroprosthetics: Theory and Practice*; World Scientific: London, 2004.
(72) Hodgkin, A. L.; Huxley, A. F. A Quantitative Description of Membrane Current and Its Application to Conduction and Excitation in Nerve. *J. Physiol.* **1952**, *117*, 500−544.
(73) Rudy, B.; Kirschenbaum, B.; Rukenstein, A.; Greene, L. Nerve Growth Factor Increases the Number of Functional Na Channels and Induces TTX-resistant Na Channels in PC12 Pheochromocytoma Cells. *J. Neurosci.* **1987**, *7*, 1613−1625.
(74) Mitra, P.; Miller, R. F. Mechanism Underlying Rebound Excitation in Retinal Ganglion Cells. *Visual Neurosci.* **2007**, *24*, 709.
(75) Guo, T.; Tsai, D.; Suaning, G. J.; Lovell, N. H.; Dokos, S. In Modeling Normal and Rebound Excitation in Mammalian Retinal Ganglion Cells. *2012 Annual Int. Conf. IEEE Eng. Med. Biol. Soc.* **2012**, 5506−5509.

DOI: 10.1021/acsnano.8b02976
ACS Nano 2018, 12, 8104−8114

(76) Delori, F. C.; Webb, R. H.; Sliney, D. H. Maximum Permissible Exposures for Ocular Safety (ANSI 2000), with Emphasis on Ophthalmic Devices. *J. Opt. Soc. Am. A* **2007**, *24*, 1250−1265.
(77) Sliney, D. H. Exposure Geometry and Spectral Environment Determine Photobiological Effects on the Human Eye. *Photochem. Photobiol.* **2005**, *81*, 483−489.
(78) Bareket, L.; Waiskopf, N.; Rand, D.; Lubin, G.; David-Pur, M.; Ben-Dov, J.; Roy, S.; Eleftheriou, C.; Sernagor, E.; Cheshnovsky, O. Semiconductor Nanorod−Carbon Nanotube Biomimetic Films for Wire-free Photostimulation of Blind Retinas. *Nano Lett.* **2014**, *14*, 6685−6692.
(79) Bahmani Jalali, H.; Trabzon, L. Structural and Optical Properties of Nitrogen-iron co-doped Titanium Dioxide Films Prepared *via* Sol-gel Dip-coating: Effect of Urea and Iron Nitrate Concentration in the Sol. *Materialwiss. Werkstofftech.* **2016**, *47*, 657−664.

DOI: 10.1021/acsnano.8b02976
ACS Nano 2018, 12, 8104−8114